

ORIGINAL ARTICLE

Open Access



A joint InSAR-GNSS workflow for correction and selection of interferograms to estimate high-resolution interseismic deformations

Hongzhi Liu^{1,2}, Lei Xie^{1,2}, Guoqiang Zhao^{1,2}, Eslam Ali³ and Wenbin Xu^{1,2*}

Abstract

Knowledge of the spatial distribution of interseismic deformations is essential to better understand earthquake cycles. The existing methods for improving the reliability of the obtained deformations often rely on visual inspection and prior model corrections that are time-consuming, labor-intensive, and do not consider the spatial distribution of interseismic deformations. Interferometric Synthetic Aperture Radar (InSAR) data provides wide-scale coverage for interseismic deformation monitoring over a wide area. However, the interseismic signal featured as millimeter-scale and long-wave deformations is often contaminated with noise. In the present study, a new workflow to correct the interferometric phase and quantitatively select interferograms is proposed to improve the accuracy of interseismic deformation measurements. Initially, the Generic Atmospheric Correction Online Service (GACOS), Intermittent Code for Atmospheric Noise Depression through Iterative Stacking (I-CANDIS), and plate model are combined to correct the atmospheric screen and long-wave ramp phase. Subsequently, the Pearson's Correlation Coefficient (PCC) between the interferometric phase and the Global Navigation Satellite System (GNSS) constrained interseismic model as well as the Standard Deviation (STD) of the interferometric phase are introduced as criteria to optimize the selection of interferograms. Finally, the intermittent stacking method is used to generate an average velocity map. A comprehensive test using Sentinel-1 images covering the Haiyuan Fault Zone validate the effectiveness of our workflow in measuring interseismic deformations. This demonstrates that the proposed joint InSAR-GNSS workflow can be extended to study the subtle interseismic deformations of major fault systems in Tibet and worldwide.

Keywords Interferometric synthetic aperture radar, GNSS, Joint workflow, Interseismic deformation, Haiyuan fault zone

Introduction

Monitoring interseismic deformations in active fault zones is necessary to understand continental deformations, earthquake cycles, and seismic hazards (Franklin & Huang, 2022; Kaneko et al., 2013). Since the 1990s, Interferometric Synthetic Aperture Radar (InSAR) has been widely used to measure interseismic deformations because of its merits of independence of time and weather, a high spatial resolution, and wide coverage (Sun et al., 2021; Taylor & Peltzer, 2006; Wright et al., 2001). Compared with other tectonic deformation types, the interseismic deformations occur in a wide area of hundreds or thousands of kilometers and are often

*Correspondence:

Wenbin Xu
wenbin.xu@csu.edu.cn

¹ School of Geoscience and Info-Physics, Central South University, Changsha 410083, China

² Key Laboratory of Metallogenetic Prediction of Nonferrous Metals and Geological Environment Monitoring Ministry of Education, Changsha 410083, China

³ Public Works Department, Geomatics Division, Faculty of Engineering, Cairo University, Giza Governorate 12613, Egypt

contaminated with long-wave signals, such as orbit and plate motion (Stephenson et al., 2022) and atmospheric phase delay (Zebker et al., 1997), resulting in low Signal-to-Noise Ratio (SNR) and the challenge to resolve. Several interseismic deformation monitoring methods have been proposed to overcome this issue and can be classified into the velocity-based and phase-based.

The velocity-based methods that use prior models (Li et al., 2022b; Qiao et al., 2022) or Global Navigation Satellite System (GNSS) observations (Li et al., 2021; Wei et al., 2010) can be used to correct interseismic InSAR observations. However, the effect of a prior model for correcting velocity field depends more on the model itself. A simple elastic model can generate imperfect corrections due to its inability to describe the actual scene (e.g., tectonic movement of the secondary buried fault or uneven deformation inside the non-rigid block (Li et al., 2015)); GNSS-based corrections can lead to the long-wavelength component mainly from GNSS observations rather than InSAR data, and this method is not applicable when the GNSS sites are sparse.

The phase-based methods, compared with the velocity-based methods, directly correct the interferograms, followed by a threshold selection procedure. Such methods can explore more details of time series deformation and are suitable for the regions with short wavelength tectonic deformations (e.g., fault creep). For example, Cavalié et al. (2008) used a joint inversion model to estimate atmospheric and orbital parameters in the interferometric phase and visually determined the base value of the interferogram structure function as the proxy of the SNR for interferogram selection. Jolivet et al. (2012) filtered the stack of interferograms using both the resolution threshold of the interferogram and base value of the structure function. A time series analysis based on the screened interferograms revealed the triggering relationship between creep acceleration and small regional earthquakes (Jolivet et al., 2013). Because the resultant interferograms with the aforementioned methods are mostly generated from winter acquisitions (Doin et al., 2009), some studies directly used the winter Synthetic Aperture Radar (SAR) images for interferometry and selected high-quality scenes by visual inspection (Huang et al., 2022; Li & Bürgmann, 2021). However, the joint inversion models for phase correction require a prior fault slip rate. The linear slope term for the orbital phase likely to contains the interseismic deformations that may underestimates the interseismic velocity. In interferogram selection, the manual selection of winter acquisitions is limited by data processing experience. Additionally, the data gap in summer limits the analysis of the long time series. The structural function obtained from the non-deformation zone does not consider the

spatial distribution of the interseismic deformations, thereby affecting interferogram selection.

To address the abovementioned shortcomings, we propose a novel method for phase correction by integrating the Generic Atmospheric Correction Online Service (GACOS), Intermittent Code for Atmospheric Noise Depression through Iterative Stacking (I-CANDIS), and plate model. The proposed workflow considers the intermittent characteristics of the conventional CANDIS method to improve the point density and correct the atmospheric phase. We also introduce the plate model to correct the long-wave phase and avoid the aliasing problem of polynomial fitting correction. Meanwhile, two quantitative indicators, the Pearson's Correlation Coefficient (PCC) between the interferometric phase and GNSS-constrained interseismic model, and the STandard Deviation (STD) of the interferometric phase are introduced to select high-quality interferograms by considering the spatial distribution of the interseismic deformations and residual noise level. We verify the proposed method in the Haiyuan Fault Zone on the northeastern margin of the Qinghai–Tibet Plateau with the Sentinel-1 and GNSS data.

Methods

Overview of the general workflow

The workflow diagram provided in Fig. 1 illustrates the proposed process chain. It contains the following three parts: (1) thematic phase corrections of the atmospheric delay and plate motion phase using external meteorological data and a physical function model; (2) interferogram selection using the interseismic model from external GNSS data, wherein two thresholds are used to quantify the SNR of the observations; and (3) the average velocity estimation from the intermittent stacking of optimized interferograms. The details of each step will be described in “[Thematic phase correction](#)” and “[Perturbational phase correction](#)” sections.

Thematic phase correction

The interseismic interferometric phase $\Delta\varphi$ measured by InSAR contains multiple terms:

$$\Delta\varphi = \varphi_{\text{def}} + \varphi_{\text{topo}} + \varphi_{\text{orb}} + \varphi_{\text{turb}} + \varphi_{\text{trop}} + \varphi_{\text{plate}} + \varphi_{\text{noise}} \quad (1)$$

where φ_{def} is the expected interseismic deformation, φ_{orb} is the residual orbital phase, φ_{topo} is the residual terrain phase, φ_{noise} is the noise, and φ_{turb} and φ_{trop} are the atmospheric turbulence and terrain-related atmospheric phase, respectively. The terrain-related atmospheric phase is season-dependent over steep terrain (Samsonov et al., 2014), but the turbulent atmospheric delay and orbital phase are random in the time domain. φ_{plate}

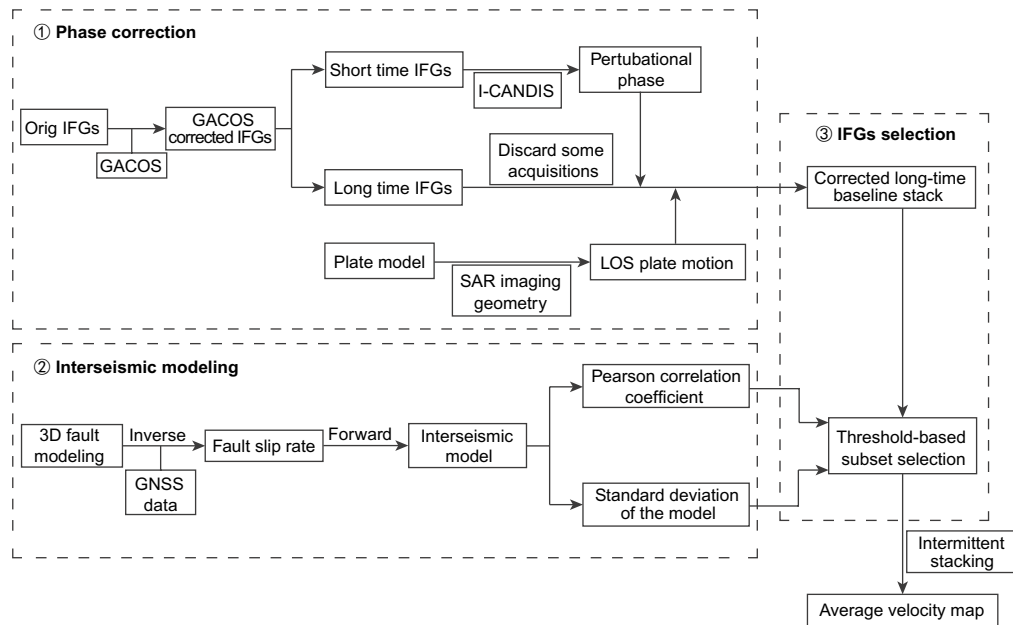


Fig. 1 Flow chart of the proposed method

denotes the phase contributed by plate motions. The long-wavelength phase generated by plate motions will impact the retrieval, modeling, and verification of interseismic deformation that should be estimated for a reliable interseismic velocity field (Stephenson et al., 2022).

Perturbational phase correction

We integrate an improved CANDIS method and GACOS (Yu et al., 2018) for perturbational phase (φ_{orb} , φ_{turb} , φ_{trop} , φ_{noise}) corrections, as the CANDIS method cannot explain the seasonal tropospheric atmospheric signal well (LI et al., 2022a) and GACOS performed well for tropospheric phase delay reduction (Wang et al., 2021).

Therefore, we first use GACOS mainly for seasonal tropospheric atmospheric delay correction. GACOS is a zenith atmospheric delay product mainly derived from the atmospheric numerical model and digital elevation model developed by the European Center for Medium-Range Weather Forecasts using the tropospheric iterative decomposition method. For each interferogram, the GACOS zenith atmospheric delay product is used to estimate the seasonal tropospheric phase using the differential and projection operations.

Then, we propose the I-CANDIS method, based on conventional CANDIS for phase correction, to increase the point density in the inhomogeneous coherent region. The phase $\Delta\varphi$ of each interferogram can be modeled as follows:

$$\Delta\varphi_{i,j} = \Delta\tau_{i,j} + \alpha_j - \alpha_i + \varepsilon_{ij} \quad (2)$$

where $\Delta\tau_{i,j}$ is the deformation phase between the acquisition time i and j (stable in time), α is the perturbational phase in each SAR image (turbulent in time), and ε represents other noises. Assuming that α -related errors are randomly distributed over time, they can be estimated and removed by the method of common point stacking, as follows:

$$\alpha_i = \frac{1}{2N} \left(\sum_{j=1, j \neq i}^N (\Delta\varphi_{i,i-j} - \Delta\varphi_{i+j,i} + \alpha_j) \right) \quad (3)$$

where N is the number of SAR images. It can be seen from Eqs. (3) that when the interferometric pixel used for stacking has non-uniform coherence, the phase estimation of the pixel will fail, thus reducing the spatial resolution of the estimated phase. To solve this problem, we adopted the intermittent coherence method for phase estimation. Before common stacking, we further divided all interferometric pixel pairs $\{\Delta\varphi_{i,i-j}, \Delta\varphi_{i+j,i} | j = 1 \sim N, j \neq i\}$ used for phase estimation. If a certain pixel pair is incoherent, this pair of pixels do not participate in the common stacking. Therefore, each pixel may have a different stacking equation, and we can set a specific threshold for the number of coherent pixel pairs to estimate the perturbational phase with different distributions. The magnitude of the quantity threshold affects the sampling density of point estimation

and the accuracy of phase estimation. The I-CANDIS method can be represented as:

$$\alpha_i = \frac{1}{2(N-k)} \left(\sum_{j \in \underbrace{\{m, \dots\}}_{N-k}, j \neq i} (\Delta\varphi_{i,i-j} - \Delta\varphi_{i+j,i} + \alpha_j) \right) \quad (4)$$

where k is the number of incoherent pixel pairs in the interferogram stack. This method can effectively increase the number of estimated perturbational phase pixels and improve their distribution, which significantly improves the capability of examining vegetated areas and the areas with inhomogeneous coherence in time.

Although the random perturbational phase can be estimated more accurately for a common scene through increasing scene numbers, a larger scene stack applies an additional linear constraint to the deformation. To avoid strong temporal-linear constraints, this method uses short-time baseline interferograms to estimate the perturbational phase of each scene. Because the phase estimation cannot be well-resolved at both ends of the stack, we discard the first and the last three, and other unresolvable acquisitions. Based on the remaining acquisitions, a long-time baseline stack is constructed, and the estimated random delays are applied to the long-time baseline interferograms for further interseismic velocity estimation.

Plate motion correction

In addition to tectonic deformation, the contribution of plate motion in the interferometric phase is corrected by the GACOS+I-CANDIS flow. The phase caused by plate motion represents the long-wave ground slope in the interferogram. This is the projection of the bulk plate motion in the satellite reference frame in the Line Of Sight (LOS) direction. The plate motion velocity V_p of X_p at any position on the plate can be derived from the Euler order Ω ($V_p = \Omega \times X_p$), that can be determined from the GNSS sites distant from the plate boundary. Therefore, the proposed method derives the bulk plate motion with the plate model (Altamimi et al., 2017) and projects it in LOS direction according to the satellite imaging geometry. Moreover, because an external independent physical model is used, the long-wave correction for the plate motion will not affect the interseismic deformation.

Interferogram selection based on an interseismic fault model

Interferograms should be selected after atmospheric and plate model corrections for an improved interseismic deformation result. In this study, the Pearson's Correlation Coefficient (PCC) (Cohen et al., 2009) between the

interferogram and interseismic model and the Standard Deviation (STD) of the interferogram are used to select

$$\text{interferograms. The PCC can be expressed as:}$$

$$R_{\text{PCC}} = \frac{\sum_m \sum_n (\varphi_{m,n} - \bar{\varphi})(\phi_{m,n} - \bar{\phi})}{\sqrt{(\sum_m \sum_n (\varphi_{m,n} - \bar{\varphi})^2)(\sum_m \sum_n (\phi_{m,n} - \bar{\phi})^2)}} \quad (5)$$

where $\varphi_{m,n}$ and $\phi_{m,n}$ represent the interferometric phase and model phase in row m and column n , respectively. $\bar{\varphi}$, and $\bar{\phi}$ represent their mean values. Accordingly, the STD of each interferogram can be expressed as:

$$S_{\text{STD}} = \sqrt{\frac{\sum_m \sum_n (\varphi_{m,n} - \bar{\varphi})^2}{m \cdot n}} \quad (6)$$

First, the interseismic model is obtained using the bayesian inversion method (Bagnardi & Hooper, 2018) based on fault geometry and GNSS observations. By setting the PCC threshold, the interferogram that is correlated with the interseismic model is selected to ensure a significant deformation gradient. Secondly, to select the interferogram with a low noise level, the STD of the interseismic deformation model (i.e., the product of the interseismic velocity model and the maximum temporal baseline of the interferogram) is another selecting criteria. To retain more interferograms with a high SNR and ensure the stability of the interferogram network, if the proportion of the selected interferograms smaller than 60%, approximately 60% of the corrected interferograms are retained based on the order of the interferogram standard deviation. As the STD changes based on both the tectonic signal and spatial noise, a lower STD indicates a lower spatial noise, and the remaining phase change is mainly caused by the deformation gradient. The interferogram selected based on the conditions of the PCC and STD can suppress the spatial noise and consider the interseismic deformation gradient signal inside the interferogram. Finally, intermittent stacking (Sowter et al., 2013) is used to generate an average interseismic deformation velocity field.

Application in the Haiyuan fault zone

Study area and data

The Haiyuan Fault Zone—an active and large left-lateral fault zone on the northeastern margin of the Qinghai-Tibet Plateau (Li et al., 2009; Qiu & Sun, 2023)—is selected as the study area. The past century witnessed destructive earthquakes with magnitudes > Mw 8 (Fig. 2).

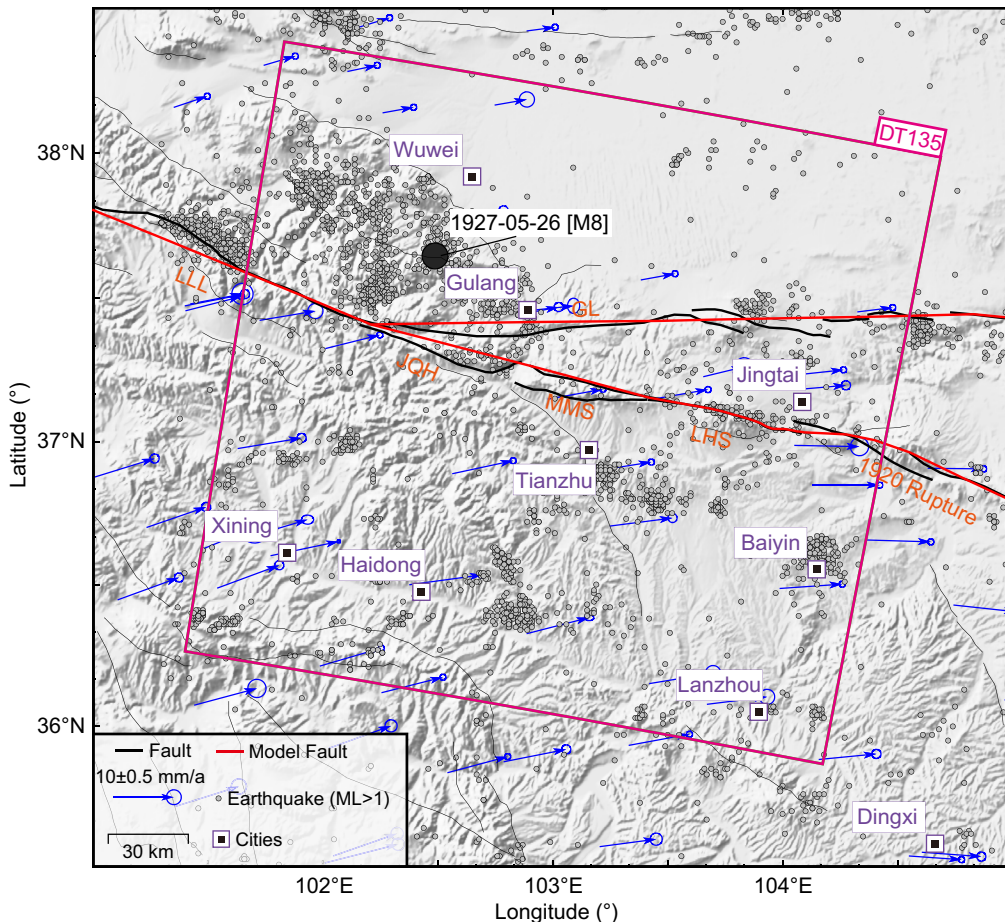


Fig. 2 Tectonic map and data coverage of the study area. Blue arrows indicate the GNSS observed displacement during 1999–2016 (Wang & Shen, 2020). Magenta rectangles represent the coverage of Sentinel-1 data in the descending orbit. Gray circles denote ML > 1 earthquakes during 1970–2021 (<http://data.earthquake.cn>), ML stands for Richter magnitude

Between the rupture area of the 1920 Mw 8.5 earthquake and the 1927 Mw 8 earthquake, a 260 km seismic gap exists in the western section of the Laohushan Segment, indicating a high potential seismic hazard (Gaudemer et al., 1995). Therefore, determining the current interseismic deformation and evaluating the strain distribution of the Haiyuan Fault Zone is important.

Sentinel-1 data acquired between Mar 19, 2015 and Nov 30, 2021, are used to construct both long-time (Group A) and short-time (Group B) baseline interferograms to monitor deformations and estimate the perturbational phases. The spatiotemporal baselines are Group A ($B_p < 90$ m, 400 d $< B_T < 500$ d) and Group B ($B_p < 200$ m, $B_T < 120$ d). B_p is the spatial perpendicular baseline, B_T is the temporal baseline.

An interseismic deformation model is constructed based on regional geological structures. Two geological traces of the active fault zone are used: Haiyuan and Gulang Fault zones. To avoid the boundary effect (Xu

et al., 2018), the width and length of the fault are set as 3000 km and 500 km, respectively. We set the locking depths of 20 km and 18 km for the Haiyuan and Gulang faults, respectively, according to the cut-off depth (96%) of the microseismic activity (Fig. 3). Since the study area is in the Eurasian plate, the Euler point $w = [-0.085, -0.531, 0.770]$ is used to derive the plate velocity field. Additionally, we use 23 GNSS sites in the study area from the Crustal Movement Observation Network of China. The coseismic and postseismic deformations are removed from the secular velocity solution (Wang & Shen, 2020).

Data processing

InSAR data processing and correction

The differential interference module in GAMMA software (Wegmüller & Werner, 1997) is used to generate interferograms. The terrain phase is simulated and eliminated using the 1 arc-sec Shuttle Radar Topography

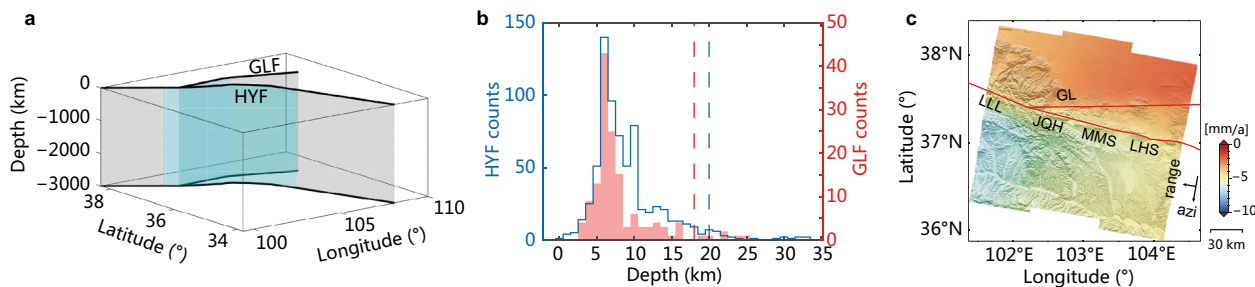


Fig. 3 Interseismic model of the Haiyuan and Gulang faults and the depth distribution of micro-seismic events. **a** 3-D fault geometry. The blue segment represents the modeling fault plane. The gray segment represents the extended fault plane to avoid the boundary effect. **b** Histogram of the micro-seismic depth. Dashed lines indicate the cut-off depths (96%). **c** Predicted deformation model in the LOS direction

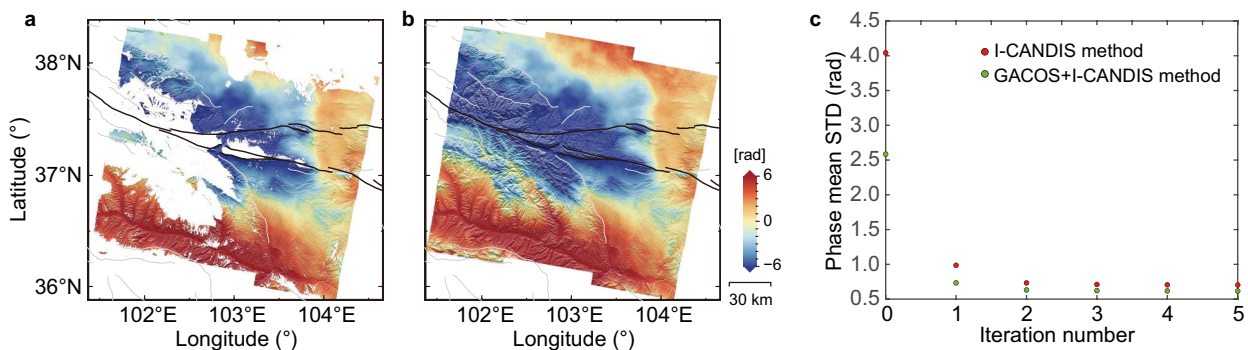


Fig. 4 Example of atmospheric phase (Sep 23, 2018) derived from **a** standard CANDIS and **b** I-CANDIS. **c** The mean STD of Group B interferograms obtained by multiple iterations of I-CANDIS (red point) and GACOS + I-CANDIS (green point)

Mission digital elevation model (Farr et al., 2007). Moreover, a 30×7 spatial multi-look operator (range \times azimuth) is used to improve the computational efficiency and suppress the phase noise. Classical Goldstein filtering (Goldstein & Werner, 1998) is used to filter the multi-look interferogram, and phase unwrapping is performed based on the minimum-cost flow method.

To illustrate the advantages of I-CANDIS and the combined GACOS correction, we set the threshold of coherent pixel pairs to 1, and as shown in Fig. 4a, b, compared with CANDIS, I-CANDIS significantly increases the spatial sampling of the estimated phase. The mean spatial sampling of the atmospheric phase estimated by the I-CANDIS method is 28% higher than that estimated by CANDIS. Moreover, the mean STD of the I-CANDIS correction for Group B interferograms corrected by GACOS is lower than that of the I-CANDIS correction without GACOS (Fig. 4c). Since the mean STD of the interferogram changed slightly (< 0.03 rad) after two iterations, we chose two rounds of I-CANDIS corrections.

As illustrated in Fig. 5, the proposed thematic phase correction method significantly improves the SNR of the interference phase in Group A. Approximately 91% of the interferograms showed a decrease in STD, with a mean

reduction in STD of 30% after GACOS corrections. The combined GACOS + I-CANDIS phase correction results show that nearly all interferograms exhibit reduction, and the mean STD reduction rate increased roughly twofold, reaching 62%. Moreover, the plate model correction provides a further improvement of approximately 5%, avoiding the problem of interseismic deformation absorbed by polynomial fitting. The PCC between the corrected interferogram and the interseismic model obtained by polynomial fitting is 0.03 (Fig. 6i), while that of the corrected interferogram after plate motion correction reaches 0.49 (Fig. 6g).

Interferogram selection and velocity field estimation

By setting the PCC to 0.45, 44% of the interferograms are retained from the original stack (Fig. 7a). The rejected interferograms typically show significant residual ramps or invisible deformation gradients across the fault zone (Fig. 7b, c). The first and second interferograms (Fig. 7b) are rejected because the threshold for neither the correlation nor the STD is met. Therefore, the interferograms contain only large atmospheric residuals without any deformation signals. Furthermore, the third and fourth interferograms (Fig. 7b) are rejected because they do

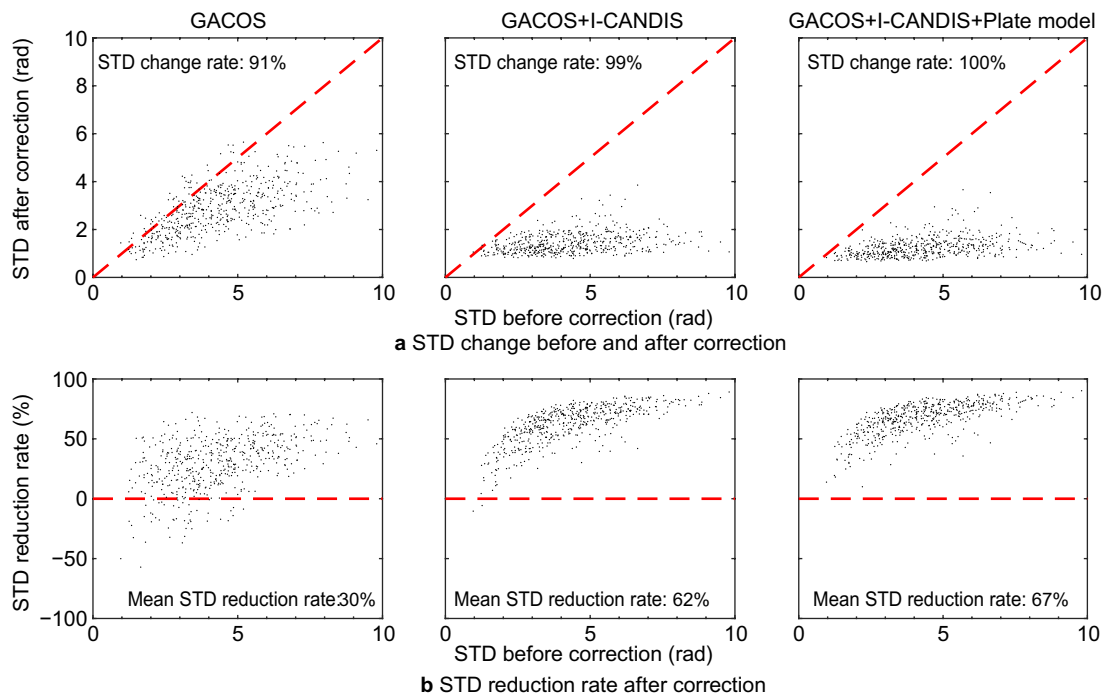


Fig. 5 a Change in STD. b) STD reduction rate of all pixels in each interferogram resulting from the application of different correction methods. The correction methods are marked at the top of each column. Each black dot represents an interferogram. The percentages of interferograms with (a) reduced STD after correction are provided at the top left of each subpanel, and b mean values of STD reduction rate are provided at the down right of each subpanel

not meet the STD threshold. These interferograms show the deformation gradients across the fault. However, the influence of the unwrap error or long-wave atmosphere is significant, leading to a bias in the target deformation signals. Similarly, the fifth and sixth interferograms (Fig. 7b) are discarded because the interseismic model and observation data are weakly correlated due to the dominant atmospheric residues of local turbulence and long-wave artifacts. Finally, the number of intermittent coherent pixels is set to 100 for the generation of a velocity field with the intermittent stacking method.

Results and discussion

The interseismic deformation estimated with the proposed method shows a significant gradient change across the Haiyuan Fault (Fig. 8). The cross-fault variation in the deformation field is consistent with the left-lateral strike-slip of the Haiyuan Fault. The narrow velocity discontinuity near the Laohushan Fault indicates a continuous shallow creep. The profile PP' (Fig. 8b) also shows a signal superposition of the interseismic tectonic motion and a shallow creep. Using a simple elastic dislocation model (Segall, 2010), the slip rate of the Laohushan Fault Zone is approximately 4.4 mm/a and the creep rate is approximately 2.8 mm/a, indicating that the shallow part

of the Laohushan Fault Zone has a slip deficit. Moreover, the slip rate of the Gulang Fault Zone is approximately 3.4 mm/a. The inversion results are consistent with the previous studies within the uncertainty range (Liu et al., 2018; Zhang et al., 2019), which confirms the reliability of our deformation field. Some local subsidence signals (e.g., north of the Gulang Fault Zone) may be associated with mining, groundwater extraction, and other human activities.

To further evaluate the effectiveness of the proposed method and the accuracy of the velocity field, we compare the velocity fields obtained using the uncorrected stacking method, the corrected stacking method, and the network correction method from Cavalie et al. (2008) (Fig. 9a–c) with our proposed method (Fig. 9d). The uncorrected stacking result is notably disturbed by the strong atmospheric phase, and the interseismic strain accumulation across the fault is superimposed by these problematic terms leading to the largest STD of 2.9 mm/a and the lowest PCC of 0.42 (Fig. 9a). The corrected stacking result shows the improvements in STD and PCC, and interseismic deformation is retained (Fig. 9b). This indicates that the phase-correct method can effectively restore the deformations and suppress the regional atmospheric disturbances. However, the

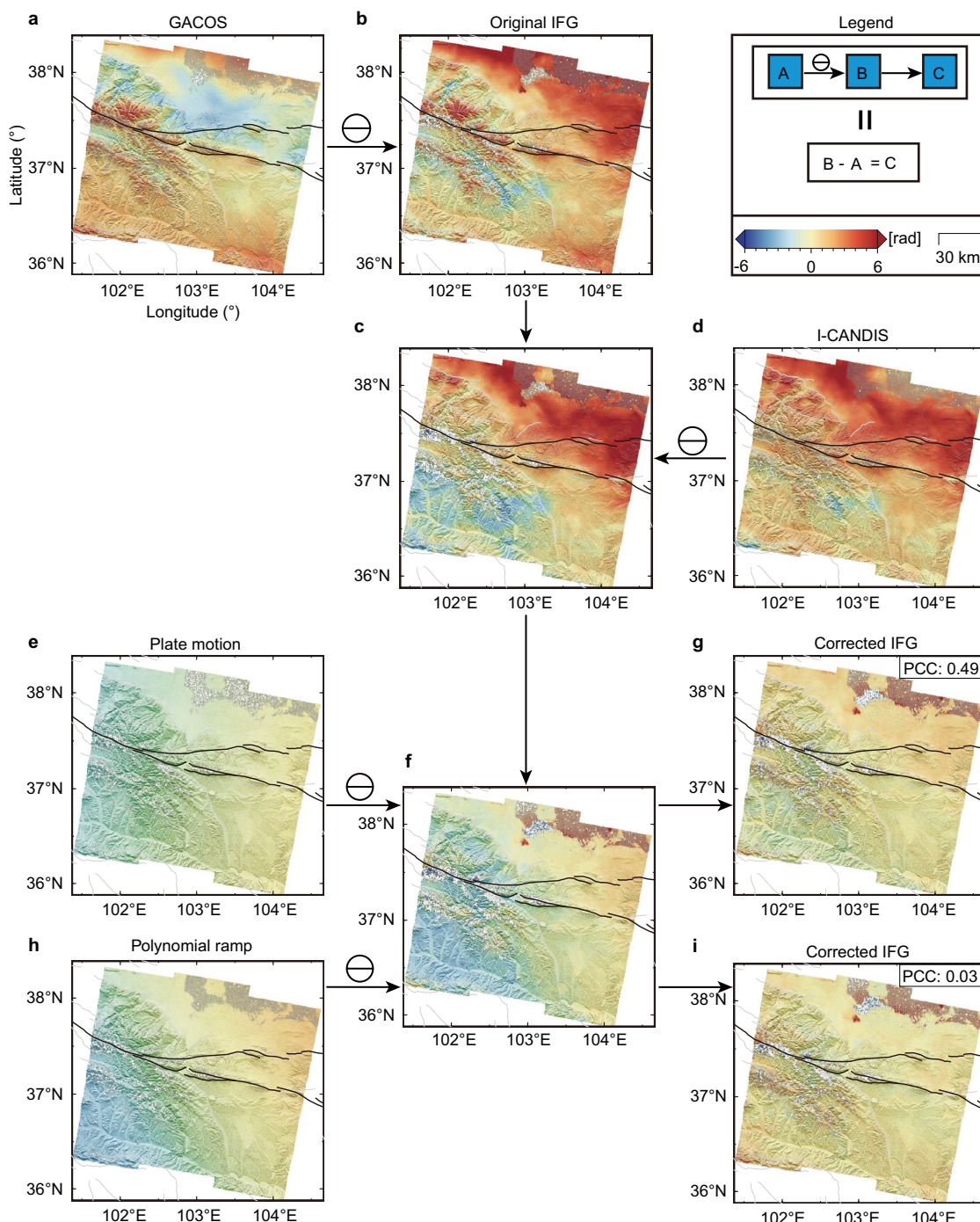


Fig. 6 Example of interferogram corrections and different phase components (Oct 05, 2018–Jan 16, 2020). **a** Atmospheric phase from GACOS. **b** Original interferogram. **c** Interferogram corrected with GACOS. **d** Perturbational phase from I-CANDIS. **e** Phase of plate motion derived by the plate model. **f** Interferogram corrected with the GACOS + I-CANDIS. **g** Interferogram corrected with GACOS + I-CANDIS + Plate model. **h** The phase ramp obtained by the first-order polynomial fitting. **i** Interferogram corrected with GACOS + I-CANDIS + Polynomial ramp. The upper right of the interferograms, **g** and **i**, is the PCC value between the interferogram and the interseismic model. The legend represents the deformation color bar, scale bar, and the mathematical symbol for the correction process

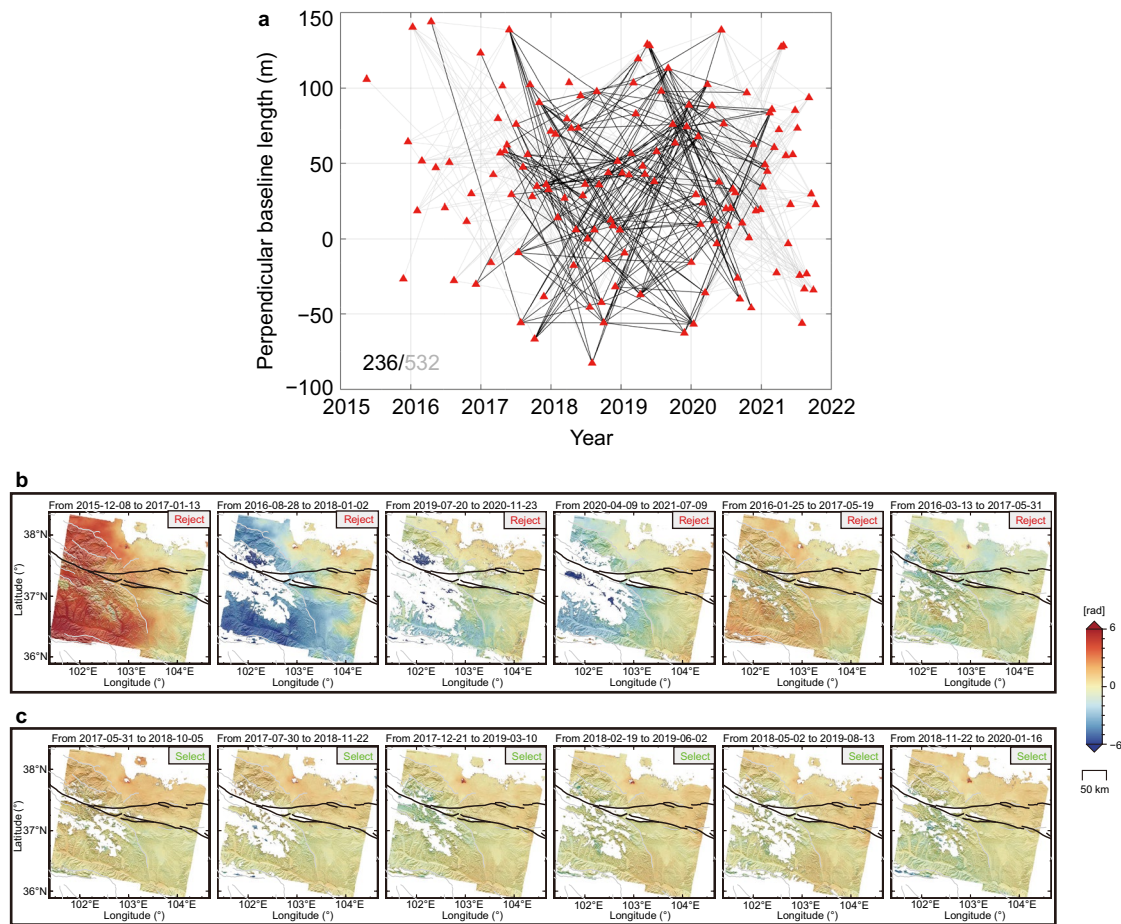


Fig. 7 Results of interferogram selection. **a** Network configurations of descending observations. Red triangles represent the time epochs of SAR data. Gray and black lines represent the discarded and selected interferograms, respectively. **b** Examples of selected interferograms. **c** Examples of rejected interferograms

long-wave disturbances still exist in the corrected velocity field (Fig. 9b). The network-based correction method cannot suppress the topography-related atmosphere (Fig. 9c), which leads to a low PCC to the model prediction and significant velocity fluctuation along the fault. The results obtained using the proposed method (Fig. 9d) show it can effectively suppress the remaining long-wave phase and regional erroneous phases. Quantitatively, the velocity field obtained from the stacked network method has a large Root Mean Square Error (RMSE) value for the difference of GNSS horizontal observations of 1.7 mm/a (Fig. 9e). Our method can decrease the RMSE with all interferograms to 0.9 mm/a, and the proposed interferogram selection can further decrease the residual to 0.6 mm/a. The QQ' profile also shows that the fluctuation along the fault strike is further suppressed from 2.3 to 0.25 mm/a over a distance of 100 km (Fig. 9f).

In addition, we compare the proposed interferogram selection method with the energy noise based method

(referred to selection method (1) (Cavalié et al., 2008) and the energy noise and resolution combined method (referred to select method (2) (Jolivet et al., 2012)). We setup the criteria for interferogram selection method according to the above studies. For selection method 1: we chose $S(30)/B_T > 2$ rad for each interferogram, where $S(30)$ represents the spatially correlated noise level of interferograms within 30 km. For selection method 2: we chose $S(30) < 1$ rad and the resolution threshold to be less than 0.75 for each SAR acquisition. The estimated interseismic velocity maps using these two methods are basically the same, with only slight differences in the slope along the fault, and our method outperforms these two methods with 5% and 30% of increase in correlation coefficient and consistency with GNSS.

In interferogram selection, micro-seismic depth is selected to determine the locking depth of the fault and forward inverse of the interseismic model. This methodology has the following two advantages. One is sparse

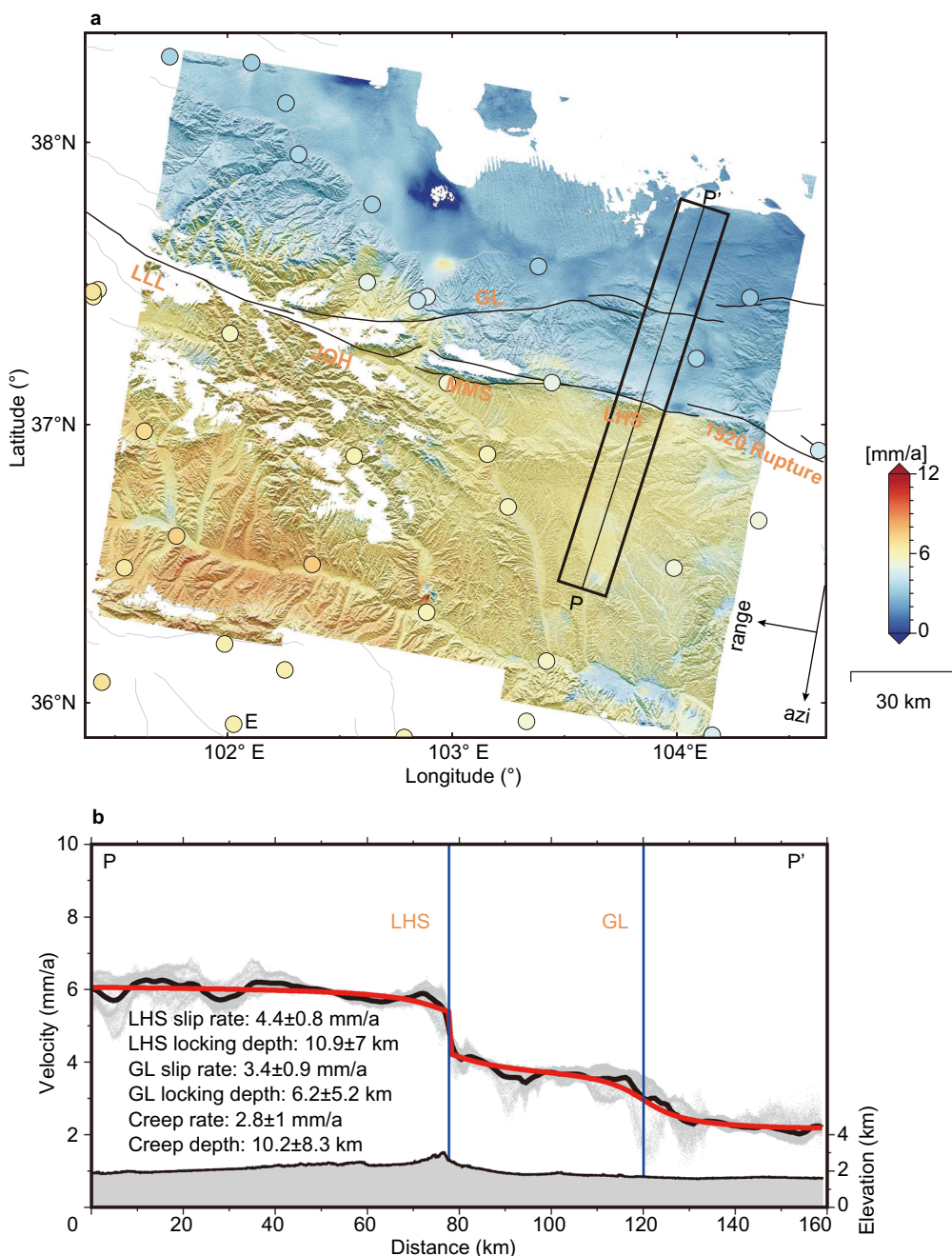


Fig. 8 **a** Interseismic velocity map determined with the proposed method. The colored dots represent the GNSS velocity field. **b** Velocity profile (PP') across the Haiyuan Fault Zone. Black dots represent binned average values every 0.7 km along the profile, and the red line represents the model predictions with the bayesian inversion

GNSS observations can not capture the continuous deformations near the fault, making it difficult to constrain the locking depth. The other is the interseismic model can be estimated according to the microseismic distribution and geological slip rate, which are more flexible and can easily be extended to other locations.

Owing to the advantages of the proposed phase correction method, only few interferograms are remarkably affected by atmospheric changes in the corrected interferogram. When the number of interferograms is large, their selection does not significantly influence the derived average deformation rate field. However,

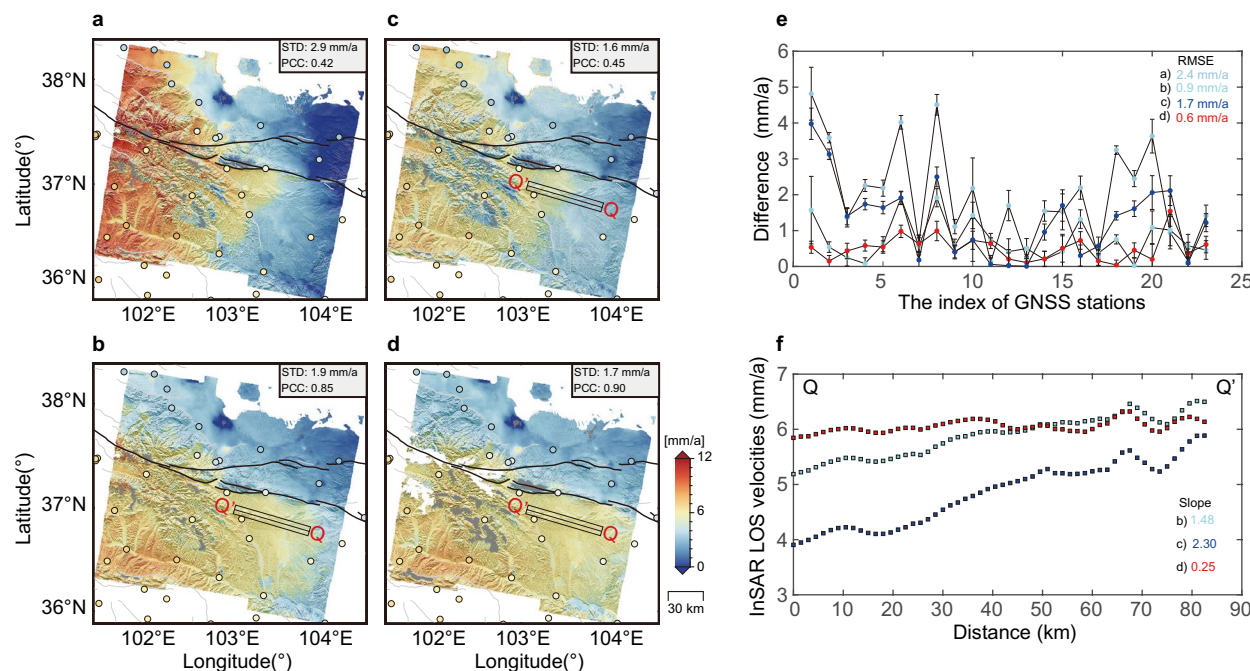


Fig. 9 Comparison and verification of interseismic deformations obtained with different methods. **a** and **b** Results of the total set of uncorrected and corrected interferograms, respectively. STD and PCC of the results are shown in the upper right corner. **c** Result from network-based method. **d** Result from the proposed method. **e** Comparison of InSAR and GNSS observations. **f** Velocities along the profile QQ'. The squares represent binned average values every 1.5 km along the profile. The unit of the profile slope is mm/a/100 km

interferogram selection uses fewer interferogram sets and results in better average deformation velocity field results compared to that all interferogram superposition methods are used together, thereby improving the computational efficiency and SNR of the deformation field.

Conclusions

In this study, an InSAR interseismic deformation monitoring method is proposed based on the framework flow of phase correction and interferogram selection. It has the following advantages: (1) GACOS and CANDIS can be integrated to effectively correct the phase when considering the different spatiotemporal characteristics of seasonal stratified tropospheric delays and turbulent atmosphere. The I-CANDIS is proposed to replace CANDIS to further increase the sampling density of the estimated perturbational phase; (2) A plate model can be applied to decrease the residual long-wave signal in the interferograms, which avoids the problem of interseismic deformation absorbed by polynomial fitting; (3) The interseismic deformation model (i.e., PCC and STD) can be used to optimize the interferogram selection and reduce the computational costs.

Furthermore, the evaluation of the method is conducted in the Haiyuan Fault Zone using the Sentinel-1 data. The results show that the estimated interseismic deformation field can describe the deformation characteristics of the slow gradient across the fault zone. Several experiments, including the fault kinematic parameters of inversion, a comparison with GNSS velocity fields, the slope estimation sampled along the fault, and a comparison with existing correction methods, demonstrates the good performance and effectiveness of the proposed method.

Acknowledgements

The figures were prepared using the public domain Generic Mapping Tools and MATLAB. Sentinel-1A data were provided by European Space Agency.

Author contributions

W.X conceptualize the study. H.L. and L.X process the data and write the original paper with the support of W.X. G.Z, and E.A. All authors contribute in revision and approved the final manuscript.

Funding

This work was supported by the National Natural Science Foundation of China (42174023). Frontiers cross research project of Central South University (Grant number: 2023QYJC006).

Availability of data and materials

The datasets used and analyzed in this study are available from the corresponding author on reasonable request.

Declarations

Competing interests

The authors declare that they have no competing interests.

Received: 21 December 2022 Accepted: 8 May 2023

Published online: 05 June 2023

References

- Declarations**

Competing interests
The authors declare that they have no competing interests.

Received: 21 December 2022 Accepted: 8 May 2023
Published online: 05 June 2023

References

Altamimi, Z., Métivier, L., Rebischung, P., et al. (2017). ITRF2014 plate motion model. *Geophysical Journal International*, 209(3), 1906–1912. <https://doi.org/10.1093/gji/ggx136>

Bagnardi, M., & Hooper, A. (2018). Inversion of surface deformation data for rapid estimates of source parameters and uncertainties: A Bayesian approach. *Geochemistry, Geophysics, Geosystems*, 19(7), 2194–2211. <https://doi.org/10.1029/2018GC007585>

Cavalie, O., Lasserre, C., Doin, M. P., et al. (2008). Measurement of interseismic strain across the Haiyuan fault (Gansu, China), by InSAR. *Earth and Planetary Science Letters*. <https://doi.org/10.1016/j.epsl.2008.07.057>

Cohen, I., Huang, Y., Chen, J., et al. (2009). Pearson correlation coefficient. Noise reduction in speech processing, pp. 1–4.

Doin, M. P., Lasserre, C., Peltzer, G., et al. (2009). Corrections of stratified tropospheric delays in SAR interferometry: Validation with global atmospheric models. *Journal of Applied Geophysics*. <https://doi.org/10.1016/j.jappgeo.2009.03.010>

Farr, T. G., Rosen, P. A., Caro, E., et al. (2007). The Shuttle Radar Topography Mission. *Reviews of geophysics*, 45(2). doi:https://doi.org/10.1029/2005R_G000183

Franklin, K. R., & Huang, M.-H. (2022). Revealing crustal deformation and strain rate in taiwan using InSAR and GNSS. *Geophysical Research Letters*. <https://doi.org/10.1029/2022GL101306>

Gaudemer, Y., Tapponniere, P., Meyer, B., et al. (1995). Partitioning of crustal slip between linked, active faults in the eastern Qilian Shan, and evidence for a major seismic gap, the 'Tianzhu gap', on the western Haiyuan Fault, Gansu (China). *Geophysical Journal International*, 120(3), 599–645. <https://doi.org/10.1111/j.1365-246X.1995.tb01842.x>

Goldstein, R. M., & Werner, C. L. (1998). Radar interferogram filtering for geophysical applications. *Geophysical Research Letters*, 25(21), 4035–4038. <https://doi.org/10.1029/1998GL900033>

Huang, Z., Zhou, Y., Qiao, X., et al. (2022). Kinematics of the ~ 1000 km Haiyuan fault system in northeastern Tibet from high-resolution Sentinel-1 InSAR velocities: Fault architecture, slip rates, and partitioning. *Earth and Planetary Science Letters*, 583, 117450. <https://doi.org/10.1016/j.epsl.2022.117450>

Jolivet, R., Lasserre, C., Doin, M. P., et al. (2012). Shallow creep on the Haiyuan fault Gansu China revealed by SAR Interferometry. *Journal of Geophysical Research Solid Earth*. <https://doi.org/10.1029/2011JB008732>

Jolivet, R., Lasserre, C., Doin, M. P., et al. (2013). Spatio-temporal evolution of aseismic slip along the Haiyuan fault, China: Implications for fault frictional properties. *Earth and Planetary Science Letters*, 377–378, 23–33. <https://doi.org/10.1016/j.epsl.2013.07.020>

Kaneko, Y., Fialko, Y., Sandwell, D. T., et al. (2013). Interseismic deformation and creep along the central section of the North Anatolian Fault (Turkey): InSAR observations and implications for rate-and-state friction properties. *Journal of Geophysical Research: Solid Earth*, 118(1), 316–331. <https://doi.org/10.1029/2012JB009661>

Li, C., Zhang, P.-Z., Yin, J., et al. (2009). Late Quaternary left-lateral slip rate of the Haiyuan fault, northeastern margin of the Tibetan Plateau. *Tectonics*. <https://doi.org/10.1029/2008TC002302>

Li, S., Dong, J., Zhang, L., et al. (2022a). Time-series InSAR tropospheric atmospheric delay correction based on common scene stacking. *National Remote Sensing Bulletin*. <https://doi.org/10.11834/jrs.20221736>

Li, S., Xu, W., & Li, Z. (2022b). Review of the SBAS InSAR Time-series algorithms, applications, and challenges. *Geodesy and Geodynamics*, 13(2), 114–126. <https://doi.org/10.1016/j.geod.2021.09.007>

Li, Y., & Bürgmann, R. (2021). Partial coupling and earthquake potential along the Xianshuise fault China. *Journal of Geophysical Research: Solid Earth*. <https://doi.org/10.1029/2020JB021406>

Li, Y., Nocquet, J. M., Shan, X., et al. (2021). Geodetic observations of shallow creep on the Laohushan-Haiyuan fault, northeastern tibet. *Journal of Geophysical Research: Solid Earth*, 126(6), e2020JB021576. <https://doi.org/10.1029/2020JB021576>

Li, Y., Qu, C., Shan, X., et al. (2015). Deformation of the Haiyuan-Liupanshan fault zone inferred from the denser GPS observations. *Earthquake Science*, 28(5), 319–331. <https://doi.org/10.1007/s11589-015-0134-z>

Liu, J., Ren, Z., Zhang, H., et al. (2018). Late Quaternary slip rate of the Laohushan fault within the Haiyuan fault zone and its tectonic implications. *Chinese Journal of Geophysics*, 61(4), 1281–1297. <https://doi.org/10.6038/cjg2018L0364>

Qiao, X., Zhou, Y., & Zhang, P. (2022). Along-strike variation in fault structural maturity and seismic moment deficits on the Yushu-Ganzi-Xianshuise fault system revealed by strain accumulation and regional seismicity. *Earth and Planetary Science Letters*, 596, 117799. <https://doi.org/10.1016/j.epsl.2022.117799>

Qiu, J., & Sun, J. (2023). Characteristics of normal-fault earthquake deformation in the Qinghai-Tibet Plateau revealed by InSAR. *Reviews of Geophysics and Planetary Physics*. <https://doi.org/10.19975/j.dqxx.2022-079>

Samsonov, S. V., Trishchenko, A. P., Tiampo, K., et al. (2014). Removal of systematic seasonal atmospheric signal from interferometric synthetic aperture radar ground deformation time series. *Geophysical Research Letters*, 41(17), 6123–6130. <https://doi.org/10.1002/2014GL061307>

Segall, P. (2010). *Earthquake and volcano deformation*. Princeton University Press.

Sowter, A., Bateson, L., Strange, P., et al. (2013). DInSAR estimation of land motion using intermittent coherence with application to the South Derbyshire and Leicestershire coalfields. *Remote Sensing Letters*, 4(10), 979–987. <https://doi.org/10.1080/2150704X.2013.823673>

Stephenson, O. L., Liu, Y.-K., Yunjun, Z., et al. (2022). The impact of plate motions on long-wavelength insar-derived velocity fields. *Geophysical Research Letters*. <https://doi.org/10.1029/2022GL099835>

Sun, K., Meng, G. J., Hong, S. Y., et al. (2021). Interseismic movement along the Luhuo-Daofu section of the Xianshuise Fault from InSAR and GPS observations. *Chinese Journal of Geophys (in Chinese)*, 64(7), 2278–2296. <https://doi.org/10.6038/cjg202100364>

Taylor, M., & Peltzer, G. (2006). Current slip rates on conjugate strike-slip faults in central Tibet using synthetic aperture radar interferometry. *Journal of Geophysical Research: Solid Earth*. <https://doi.org/10.1029/2005JB004014>

Wang, M., & Shen, Z.-K. (2020). Present-day crustal deformation of continental China derived from GPS and Its tectonic implications. *Journal of Geophysical Research: Solid Earth*. <https://doi.org/10.1029/2019JB018774>

Wang, Y., Chang, L., Feng, W., et al. (2021). Topography-correlated atmospheric signal mitigation for InSAR applications in the Tibetan plateau based on global atmospheric models. *International Journal of Remote Sensing*, 42(11), 4361–4379. <https://doi.org/10.1080/01431161.2021.1892856>

Wegmüller, U., & Werner, C. (1997). Gamma SAR processor and interferometry software. *ESA SP (Print)*, 1687–1692.

Wei, M., Sandwell, D., & Smith-Konter, B. (2010). Optimal combination of InSAR and GPS for measuring interseismic crustal deformation. *Advances in Space Research*, 46(2), 236–249. <https://doi.org/10.1016/j.asr.2010.03.013>

Wright, T., Parsons, B., & Fielding, E. (2001). Measurement of interseismic strain accumulation across the North Anatolian Fault by satellite radar interferometry. *Geophysical Research Letters*, 28(10), 2117–2120. <https://doi.org/10.1029/2000GL012850>

Xu, W., Wu, S., Materna, K., et al. (2018). Interseismic ground deformation and fault slip rates in the greater san francisco bay area from two decades of space geodetic data. *Journal of Geophysical Research: Solid Earth*, 123(9), 8095–8109. <https://doi.org/10.1029/2018JB016004>

Yu, C., Li, Z., & Penna, N. T. (2018). Interferometric synthetic aperture radar atmospheric correction using a GPS-based iterative tropospheric decomposition model. *Remote Sensing of Environment*, 204, 109–121. <https://doi.org/10.1016/j.rse.2017.10.038>

Zebker, H. A., Rosen, P. A., & Hensley, S. (1997). Atmospheric effects in interferometric synthetic aperture radar surface deformation and topographic maps. *Journal of Geophysical Research: Solid Earth*, 102(B4), 7547–7563.

Zhang, Y. P., Zheng, W. J., Zhang, D.-L., et al. (2019). Late Pleistocene left-lateral slip rates of the Gulang Fault and its tectonic implications in eastern Qilian Shan (NE Tibetan Plateau), China. *Tectonophysics*, 756, 97–111. <https://doi.org/10.1016/j.tecto.2019.02.013>

Publisher's Note

Springer Nature remains neutral with regard to jurisdictional claims in published maps and institutional affiliations.

Submit your manuscript to a SpringerOpen® journal and benefit from:

- Convenient online submission
- Rigorous peer review
- Open access: articles freely available online
- High visibility within the field
- Retaining the copyright to your article

Submit your next manuscript at ► springeropen.com
